Functional Acoustic Metamaterial Using Shortcut to Adiabatic Passage in Acoustic Waveguide Couplers

Shuai Tang,[1] Jin-Lei Wu[ORCID],[2,*] Cheng Lü,[1] Jie Song[ORCID],[1] and Yongyuan Jiang[1,2,3,4,5,†]

[1]*School of Physics, Harbin Institute of Technology, Harbin 150001, China*

[2]*Department of Optoelectronics Science, Harbin Institute of Technology, Weihai 264209, China*

[3]*Collaborative Innovation Center of Extreme Optics, Shanxi University, Taiyuan 030006, China*

[4]*Key Lab of Micro-Optics and Photonic Technology of Heilongjiang Province, Harbin 150001, China*

[5]*Key Lab of Micro-Nano Optoelectronic Information System, Ministry of Industry and Information Technology, Harbin 150001, China*

Shortcut to adiabatic passage (STAP), initially proposed to accelerate adiabatic quantum-state transfer, has been widely explored and applied in quantum optics and integrated optics. Here we bring STAP into the field of acoustics to design compact couplers and functional metamaterial. The space-varying coupling strengths of acoustic waveguides (WGs) are tailored by means of dressed states in a three-level system, accounting for the desirable acoustic energy transfer among three WGs with short length. We show that the acoustic coupler has a one-way feature when loss is introduced into the intermediate WG. More uniquely, when the propagation of acoustic wave is designed to mimic a Hadamard transformation, an acoustic metamaterial can be constructed by arraying several couplers, possessing the beam-splitting function and unidirectional, broadband performances. Our work bridges STAP and the acoustic coupler as well as metamaterial, which may have profound impacts on exploring quantum technologies for promoting advanced acoustic devices.

I. INTRODUCTION

Coherent control of quantum states plays a significant role in extensive practical applications including quantum-information processing [1], high-precision measurement [2], and manipulation of atoms and molecules [3]. To robustly obtain a target state with high fidelity, adiabatic passage (AP) as well as its variants has been demonstrated as an effective means through well-tuned radiative interactions [4–8], while suffering from lengthy evolution owing to the limitation of adiabatic criterion. Recently, methods for speeding up AP, called shortcut to adiabatic passage (STAP), provide approaches for rendering a system to reach the desired state quickly, accurately, and robustly [9–12]. The development of STAP makes it applicable widely from quantum optics [13–17] and integrated optics [18–22] to mechanical engineering [23,24], physical chemistry [25,26], and biology [27,28]. In this work, we intend to apply STAP for designing compact couplers and functional metamaterial in the field of acoustics.

An acoustic waveguide (WG) coupler always serves as a functional device to achieve power transfer [29–33], mode

conversion [34–36], or phase inversion [37–39] by taking advantage of the phononic crystals [40–42], Helmholtz resonators [43,44], or coiling-up particles [45–48]. Various fascinating phenomena, including focusing beam [49–53], splitting beam [31,48], self-bending beam [54,55], and vortex beam [56–58], can be observed by constructing acoustic devices integrated by WG couplers. Nevertheless, complicated structural designs pose challenges to modeling and analysis inevitably. Besides, the performance of device is subject to the narrow band and single function, hindering the practicability and industrialization of acoustic couplers. In the past decade, the combination of acoustic systems with other concepts (such as topological state [59–64], parity-time symmetry [65–68], quantum adiabaticity [69–72], and Landau-Zener transition [73]) has received great interest and has led to surprising advantages for designing advanced functional acoustic metadevices. As a promising and pragmatic quantum technology, yet STAP in an acoustic system has not been reported so far.

In this work, a technique of STAP is introduced to design compact acoustic WG couplers. Due to the agreement in form between the Schrödinger equation in quantum mechanics and the coupled-mode equation of classical waves [74], the coupled WGs for transporting energy of classical wave can be mapped to quantum states with

————————
*wujl@hit.edu.cn
†jiangyy@hit.edu.cn

transitions being driven by external fields. The propagation of acoustic wave along coupled WGs can mimic the quantum evolution controlled with STAP by meticulously modulating discrete coupling strengths between two adjacent WGs. The comparison between performances in couplers designed by STAP and AP verifies the advantage of STAP with a shorter device length. Furthermore, we show that the coupled-WG acoustic system exhibits a one-way transmission feature when introducing an appropriate loss in the intermediate WG. More uniquely, by designing a WG coupler where the propagation of acoustic wave mimics a Hadamard transformation in quantum computing, an asymmetric beam-shaping metamaterial with the beam-splitting function is able to be constructed conveniently by arraying several WG couplers. An incident plane wave can be split with a certain angle of refraction in a relatively wide space for one side incidence, but can be hardly transmitted for incidence from the other side. The present work bridges acoustic metamaterials and quantum STAP technology, providing a solution to design an advanced acoustic functional device with excellent performances.

II. AP IN AN ACOUSTIC SYSTEM OF THREE COUPLED WGS

For a three-level quantum system, as illustrated in Fig. 1(a), ladder-type transitions $|1\rangle \leftrightarrow |2\rangle$ and $|2\rangle \leftrightarrow |3\rangle$ are driven resonantly by two external fields (for example, visible laser fields for transitions of a valence electron in an atom [75]), respectively, with time-dependent Rabi frequencies $\Omega_{12}(t)$ and $\Omega_{23}(t)$. The Hamiltonian in the interaction picture under the rotating-wave approximation is written as (setting natural unit $\hbar = 1$)

$$\hat{H}(t) = \begin{pmatrix} 0 & \Omega_{12}(t) & 0 \\ \Omega_{12}(t) & 0 & \Omega_{23}(t) \\ 0 & \Omega_{23}(t) & 0 \end{pmatrix}. \quad (1)$$

The two Rabi frequencies can be parametrized by a common amplitude $\Omega(t)$ and a mixed angle $\theta(t)$, as $\Omega_{12}(t) = \Omega(t)\sin\theta(t)$ and $\Omega_{23}(t) = -\Omega(t)\cos\theta(t)$, and then instantaneous eigenstates of $\hat{H}(t)$ can be described by a unitary matrix with base vectors $\{|1\rangle, |2\rangle, |3\rangle\}$

$$U_{\mathrm{ad}} = \begin{pmatrix} \sin\theta(t)/\sqrt{2} & 1/\sqrt{2} & -\cos\theta(t)/\sqrt{2} \\ \cos\theta(t) & 0 & \sin\theta(t) \\ \sin\theta(t)/\sqrt{2} & -1/\sqrt{2} & -\cos\theta(t)/\sqrt{2} \end{pmatrix}, \quad (2)$$

where the first and third rows represent two bright states $|\varphi_\pm(t)\rangle$ with eigenenergies $E_\pm(t) = \pm\Omega(t)$, while the second row is called the dark state $|\varphi_0(t)\rangle$ with eigenenergy $E_0(t) = 0$ (the intermediate state $|2\rangle$ does not get involved in the adiabatic passage process). In the adiabatic basis, the
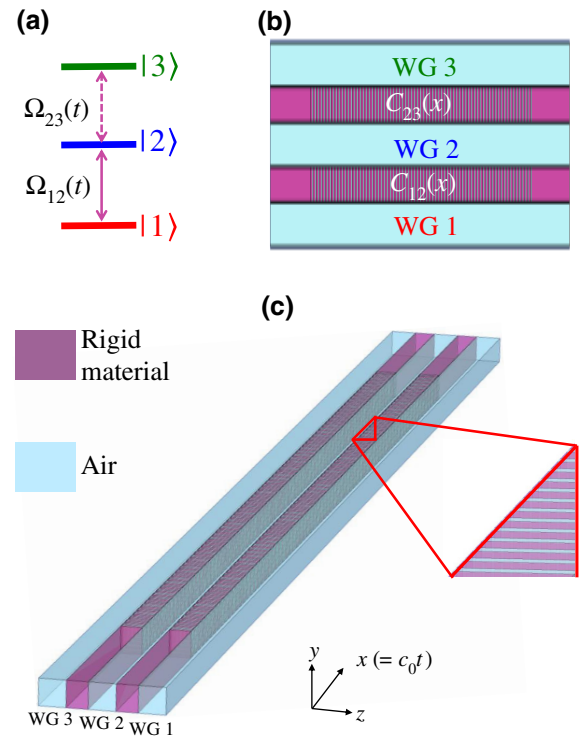

FIG. 1. (a) The three-level quantum system. The states $|1\rangle$, $|2\rangle$, and $|3\rangle$ are coupled by pump field $\Omega_{12}(t)$ and Stokes field $\Omega_{23}(t)$, respectively. (b) Acoustic three-WG coupler in the y-z plane. WGs 1 and 3 are coupled with WG 2 by space-dependent strengths $C_{12}(x)$ and $C_{23}(x)$, respectively. The purple region represents the rigid material and the cyan region represents the air background. (c) The three-dimensional schematic diagram of the acoustic three-WG system.

Hamiltonian (1) becomes

$$\hat{H}_{\mathrm{ad}}(t) = \Omega(t)\hat{M}_z + \dot{\theta}(t)\hat{M}_y, \quad (3)$$

for which three spin-1 operators are introduced

$$\hat{M}_x = \frac{1}{\sqrt{2}}\begin{pmatrix} 0 & -1 & 0 \\ -1 & 0 & 1 \\ 0 & 1 & 0 \end{pmatrix}, \quad (4a)$$

$$\hat{M}_y = \frac{1}{\sqrt{2}}\begin{pmatrix} 0 & i & 0 \\ -i & 0 & -i \\ 0 & i & 0 \end{pmatrix}, \quad (4b)$$

$$\hat{M}_z = \begin{pmatrix} 1 & 0 & 0 \\ 0 & 0 & 0 \\ 0 & 0 & -1 \end{pmatrix}. \quad (4c)$$

The term $\dot{\theta}(t)\hat{M}_y$ corresponding to nonadiabatic couplings can be ignored in the adiabatic limit $|\dot{\theta}(t)| \ll \sqrt{2}|\Omega(t)|$ [3,4,76]. Then according to the AP technique, a perfect transfer from state $|1\rangle$ to $|3\rangle$ is capable of realizing by utilizing the adiabatic medium

state $|\varphi_0(t)\rangle = \cos\theta(t)|1\rangle + \sin\theta(t)|3\rangle$, where the pulse sequence is adopted for $\theta(t_i) = 0$ and $\theta(t_f) = \pi/2$, t_i and t_f representing the start and end instants, respectively.

We would like to mimic the quantum system of three discrete levels by constructing an acoustic WG coupler and to achieve desirable energy transfer from an input WG to the target WG. The mathematical similarity of the time-dependent Schrödinger equation in quantum mechanics to the wave equation of the classical wave makes it possible to apply the AP technique in the classical-mechanics systems of coupled acoustic WGs [71,72,77]. Propagating properties in WGs of acoustic waves make typical ultra-fast phenomena in time intuitively visible in space, and also WGs of acoustic waves provide an excellent platform to investigate coherent dynamics' accessible difficultly in quantum systems.

We therefore consider an analog of the three-level model in an acoustic system. As shown in Fig. 1(b), three WGs 1, 2, and 3 for an acoustic coupler can be viewed as the discrete states $|1\rangle$, $|2\rangle$, and $|3\rangle$, respectively. The space-dependent coupling strength C_{mn} ($m = 1,2$; $n = m+1$) for transmitting sound through slits between WG m and n corresponds to the time-dependent Rabi frequency Ω_{mn} in the three-level model. Figure 1(c) shows the three-dimensional schematic of the acoustic coupler. The width of the air pipe (cyan regions) is $w_1 = 10$ mm. The thickness of rigid material (purple regions) is $w_2 = 8$ mm. The space-dependent width of the slit is $d_{mn}(x)$ between WGs m and n. The distance between two spaced slits is $p = 4$ mm. The width and height of whole waveguide are $W_0 = 46$ mm and $h = 10$ mm, respectively. By slotting the rigid wall between two adjacent WGs, WG 1 and WG 3 are coupled with WG 2 when propagating acoustic waves. The coupling strength $C_{12}(x)$ and $C_{23}(x)$ can be modulated along propagation direction (x axis) by adopting different slit widths with relation $C_{mn}(x) \propto d_{mn}(x)$, thus achieving desired space dependence.

Based on the coupled-mode theory [74], acoustic pressure fields, P_1, P_2, and P_3 satisfying normalization $\sum_{j=1}^{3} |P_j(x)|^2 = 1$, along three WGs in the coupler are described as

$$i\frac{\partial P_1(x)}{\partial x} = C_{12}(x)P_2(x),$$

$$i\frac{\partial P_2(x)}{\partial x} = C_{12}(x)P_1(x) + C_{23}(x)P_3(x), \qquad (5)$$

$$i\frac{\partial P_3(x)}{\partial x} = C_{23}(x)P_2(x),$$

which can be rewritten as a similar form of the Schrödinger equation in the spatial dimension

$$i\frac{\partial|\varphi(x)\rangle}{\partial x} = \hat{M}(x)|\varphi(x)\rangle, \qquad (6)$$

where $\hat{M}(x)$ is defined as the coupling matrix of the three-WG coupler, corresponding to the Hamiltonian of the three-level system

$$\hat{M}(x) = \begin{pmatrix} 0 & C_{12}(x) & 0 \\ C_{12}(x) & 0 & C_{23}(x) \\ 0 & C_{23}(x) & 0 \end{pmatrix}. \qquad (7)$$

The acoustic pressure at each site of coupler, $|\varphi(x)\rangle = P_1(x)|1\rangle + P_2(x)|2\rangle + P_3(x)|3\rangle$, can be calculated by solving Eq. (5). Thereafter, the AP technique for discrete quantum states in a three-level system is capable of mapping into the acoustic three-WG coupler when a spatial adiabatic criterion $|\partial\theta_s(x)/\partial x| \ll \sqrt{2}|C_s(x)|$ is satisfied, where the parameters for the spatial AP [78,79] are introduced by defining $C_{12}(x) = C_s(x)\sin\theta_s(x)$ and $C_{23}(x) = -C_s(x)\cos\theta_s(x)$, and the propagation of acoustic wave could mimic evolution of AP in quantum optics [72]. For the acoustic energy transfer from WG 1 (input port) to WG 3 (output port), one can render the sound distribution in the three WGs to follow the dark state $|\Psi_d(x)\rangle = \cos\theta_s(x)|1\rangle + \sin\theta_s(x)|3\rangle$ and set $\theta_s(x_i) = 0$ and $\theta_s(x_f) = \pi/2$, where x_i and x_f label the start and end sites of inter-WG slits, respectively.

III. STAP IN THE THREE-WG COUPLER

A. Modified coupling strengths

However, a perfect quantum-state transfer needs a very long evolution time to guarantee the temporal adiabatic criterion $|\dot{\theta}(t)| \ll \sqrt{2}|\Omega(t)|$, analogous to which an adiabatic acoustic energy transfer with criterion $|\partial\theta_s(x)/\partial x| \ll \sqrt{2}|C_s(x)|$ requires a long spatial variation of device, costing more space and resources. Therefore, it is necessary to apply a STAP technique to design inter-WG slit widths for achieving acoustic energy transfer in an compact coupler.

To shorten the length of coupled WGs, we map the time-dependent STAP technique into the space-dependent acoustic system to engineer inter-WG coupling strengths $C_{12}(x)$ and $C_{23}(x)$ as well as the coupling slits by rendering the sound distribution in the three WGs to follow a STAP pathway $|\Psi_s(x)\rangle$, a dressed state applied to achieve the desired state transfer instead of the AP pathway [i.e., the dark state $|\Psi_d(x)\rangle$]:

$$|\Psi_s(t)\rangle = \cos\mu_s(x)[\cos\theta_s(x)|1\rangle + \sin\theta_s(x)|3\rangle] \\ + i\sin\mu_s(x)|2\rangle, \qquad (8)$$

which indicates that two ports of each WG has the same sound distribution as that in the AP situation when the auxiliary parameter $\mu_s(x)$ is limited by $\mu_s(x_i) = \mu_s(x_f) = 0$. The STAP technique for a compact WG coupler requires that there are an extra pair of inter-WG coupling strengths $\tilde{C}_{12}(x)$ and $\tilde{C}_{23}(x)$ added into $C_{12}(x)$ and $C_{23}(x)$, respectively, to eliminate the transitions from $|\Psi_s(t)\rangle$ to other

orthogonal dressed states, resulting in modified inter-WG space-dependent coupling strengths $C'_{12}(x) = C_{12}(x) + \tilde{C}_{12}(x)$ and $C'_{23}(x) = C_{23}(x) + \tilde{C}_{23}(x)$. Such a pair of modified coupling strengths can be obtained by several STAP methods, such as invariant-based inverse engineering [80,81], multiple Schrödinger dynamics [82,83], transitionless evolution engineering [84,85], three-mode parallel paths [26,86], and superadiabatic dressed states [87, 88], which show different mathematical processes but similar underlying physics. In Appendix A, we give a detailed derivation for obtaining a pair of modified coupling strengths by using the STAP method of dressed states [87] in the context of the time-dependent Schrödinger equation. Accordingly, a pair of modified inter-WG space-dependent coupling strengths $C'_{12}(x)$ and $C'_{23}(x)$ for the acoustic coupler can be obtained

$$C'_{12}(x) = -\sin\theta_s(x)\cot\mu_s(x)\partial_x\theta_s(x) - \cos\theta_s(x)\partial_x\mu_s(x),$$
$$C'_{23}(x) = \cos\theta_s(x)\cot\mu_s(x)\partial_x\theta_s(x) - \sin\theta_s(x)\partial_x\mu_s(x).$$
$$(9)$$

The related parameters are set as

$$\theta_s(x) = \frac{\pi x}{2x_f} - \frac{1}{3}\sin\left(\frac{2\pi x}{x_f}\right) + \frac{1}{24}\sin\left(\frac{4\pi x}{x_f}\right),$$
$$\mu_s(x) = \frac{\beta_m}{2}\left[1 - \cos\left(\frac{2\pi x}{x_f}\right)\right],$$
$$(10)$$

for which we choose $x_0 = 0$.

B. Energy transfer from WG 1 to WG 3

To obtain the relation between the inter-WG coupling strength C and the slit width d, we consider a two-WG acoustic system composed of WGs A and B with state function $|\Psi_T(x)\rangle = A(x)|A\rangle + B(x)|B\rangle$ and the Hamiltonian $H_T(x) = C|A\rangle\langle B| + C|B\rangle\langle A|$, where $A(x)$ and $B(x)$ are the acoustic evolution waveforms along propagation direction in WG A and WG B, respectively [72,89]. Through solving the Schrödinger-like coupled-mode equation of the two-WG system $i\frac{\partial}{\partial x}|\Psi_T(x)\rangle = H_T|\Psi_T(x)\rangle$, one can obtain $|\Psi_T(x)\rangle = \exp(-iH_Tx)|\Psi_T(0)\rangle$ with $|\Psi_T(0)\rangle = A(0)|A\rangle + B(0)|B\rangle$, which yields

$$A(x) = \cos(Cx)A(0) - i\sin(Cx)B(0), \quad (11a)$$
$$B(x) = -i\sin(Cx)A(0) + \cos(Cx)B(0). \quad (11b)$$

For a given initial condition of $A(0) = A_0$ and $B(0) = 0$, the acoustic power flow along the propagation direction in WG A and WG B can be obtained as $P_A(x) = |A(x)|^2/|A_0|^2 = \cos^2(Cx)$ and $P_B(x) = |B(x)|^2/|A_0|^2 = \sin^2(Cx)$. The propagation wave between WGs A and B will funnel back and forth, leading to a periodic distribution of intensity field. The coupling strength can be

calculated by $C = \pi/L$ with L being the coupling length defined by the distance between two adjacent peaks of intensity field. In a three-WG coupler, the WGs 1 and 3 are coupled with WG 2 by space-dependent strengths $C'_{12}(x)$ and $C'_{23}(x)$ in Eq. (9), respectively. Here, $C'_{mn}(x)(m = 1, 2; n = m + 1)$ represents the space-dependent coupling strength between WGs m and n. To implement the space dependence of coupling strength $C'_{mn}(x)$, it is necessary to know how to vary the slit widths between two WGs quantificationally and accurately to change the coupling strengths in space. To this end, it is convenient to obtain the C-d correspondence from the results obtained by investigating a two-WG coupler with space-independent slit widths. According to the relation of $C = \pi/L$, we learn that the coupling strength in a two-WG system can be modulated by adopting different values of coupling length. Next, we numerically calculate the coupling length by employing a set of straight two-WG couplers with different slit widths (from 0.2 to 2 mm) at 8800 Hz, where the period of slit is set to be $p = 4$ mm. Three cases of different slit widths, $d = 0.8$, $d = 1.2$, and $d = 1.6$ mm, are shown in Fig. 2(a), while the other cases are listed in Table I. It can be seen that the coupling length decreases as the slit
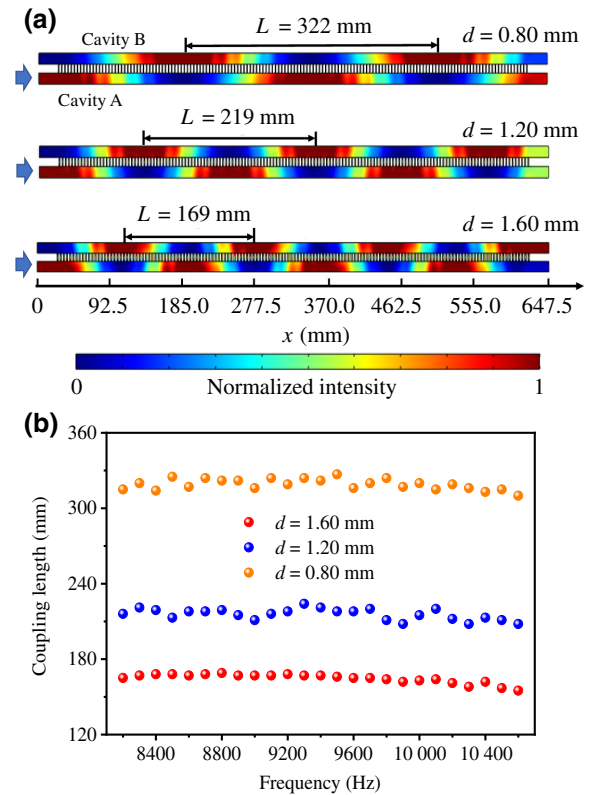

FIG. 2. (a) Acoustic intensity distributions in different acoustic couplers at 8800 Hz, for which the slit widths are $d = 0.8$, $d = 1.2$, and $d = 1.6$ mm. Blue arrows represent the input direction and location. (b) The relation between coupling length and incident frequency.

TABLE I. The coupling length (L) versus the slit width (d).

| d (mm)	L (mm)	d (mm)	L (mm)
0.2	1235	0.4	627
0.6	422	0.8	322
1.0	260	1.2	219
1.4	191	1.6	169
1.8	151	2.0	142

FIG. 3. The acoustic fields of the coupler designed by STAP for (a),(c), and by AP with shortcut evolution for (e),(g). The acoustic intensity distributions along the coupler designed by STAP for (b),(d), and by AP with shortcut evolution for (f),(h). White arrows represent the input direction and location. The working frequency is 8800 Hz.

width increases, and the relation between them can be fitted by the function $L = \alpha/d$ with $\alpha = 275$ mm^2. Therefore, the space-dependent coupling strengths of $C'_{mn}(x)$ can be achieved correspondingly by adopting different slit widths along the propagating direction of the coupler. In addition, Fig. 2(b) shows the relation between coupling length and incident frequency for the cases of $d = 0.8$, $d = 1.2$, and $d = 1.6$ mm, from which the change of coupling length is very slight within 8200–10 600 Hz, providing the foundation for the broadband feature of the three-WG coupler.

The next step is to select an appropriate value of β_m to determine the shapes of coupling strengths, so as to determine the required widths of coupling slit along propagation direction by mapping the time-dependent external fields [$\Omega'_{12}(t)$ and $\Omega'_{23}(t)$] into space-dependent coupling strength [$C'_{12}(x)$ and $C'_{23}(x)$]. As illustrated in Appendix A, the demand for maximum coupling strength decreases when the value of β_m increases, offering a variety of options for the design of coupling strengths. Meanwhile, a higher value of β_m results in a shorter evolution time (or shorter device length) with a fixed maximum coupling strength [$C_{\max} = \pi/(142$ mm$)$ for $d_{\max} = 2.0$ mm], indicating that the value of β_m is inversely related to the device length. Although a compact acoustic device needs a high value of β_m to reduce the length in space, the discrete factor should be taken into account as well because the discrete precision in the shorter device is lower than that in a longer one inevitably under a fixed slotting period, which may influence the efficiency of the acoustic energy transfer. Here, we select $\beta_m = 0.144\pi$ to ensure sufficient accuracy of discrete slit arrays, from which the device length can be calculated as $L_1 = 316$ mm. Note that we ignore the slits with $d < 0.2$ mm at both ends of the device to guarantee the feasibility of fabrication craft in practice, and the actual length of the coupler is $L_1 = 260$ mm in this case. To verify the energy-transfer feature of the acoustic coupler designed by STAP, the finite-element method is adopted to simulate the intensity distribution along each WG at 8800 Hz. The rigid materials are set as hard boundary conditions, and the ports of each WG are set as planar-wave radiation conditions. As shown in Fig. 3(a), the acoustic wave input from the left side of WG 1 can transfer to the right side of WG 3 eventually with $L_1 = 260$ mm. The
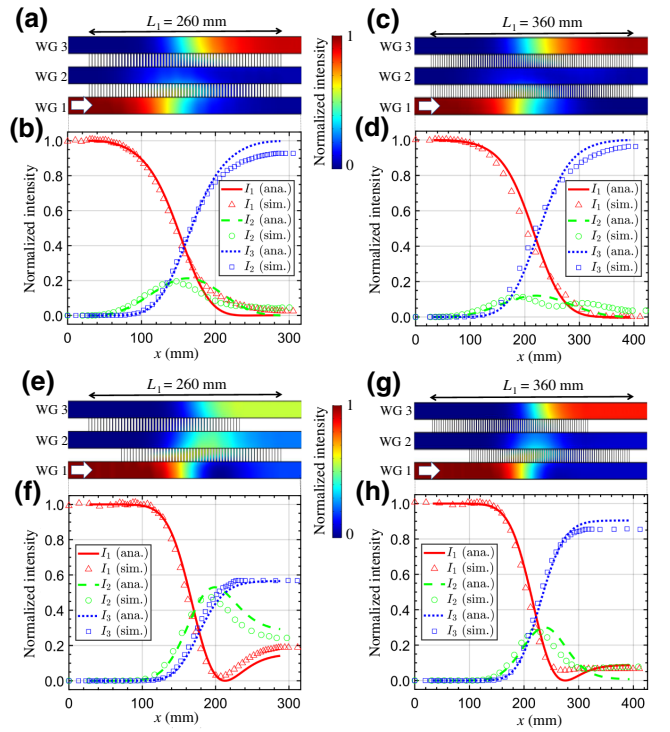
simulated intensity distributions along three WGs shown in Fig. 3(b) agree with the analytical results obtained by solving Schrödinger-like equation, Eq. (6), which confirms the feasibility of our design. It is notable that the small discrepancies between simulated and analytical results are attributed to the discrete precision, which can be diminished by lengthening the device. As shown in Figs. 3(c) and 3(d), near-perfect energy transfer can be realized as well in the acoustic coupler designed by STAP with actual length of $L_1 = 360$ mm ($\beta_m = 0.107\pi$), and the simulated intensity results fit further well with the analytical ones. In addition, the maximum acoustic intensity along WG 2 with $L_1 = 260$ mm is higher than that with $L_1 = 360$ mm, which verifies the conclusion obtained by Eq. (8) that a higher value of β_m leads to a large intensity distribution in WG 2.

On the other hand, we show the acoustic coupler designed by AP with shortcut evolution in comparison with the performance of the coupler designed by STAP. As we discuss in Sec. II, a perfect adiabatic transfer from state $|1\rangle$ to $|3\rangle$ is capable of realizing by utilizing the medium state $|\varphi_0(t)\rangle = \cos\theta(t)|1\rangle + \sin\theta(t)|3\rangle$ with $\theta(t_i) = 0$ and $\theta(t_f) = \pi/2$, which can be mapped into space dimension

as well [72]. As shown in Ref. [72], to achieve the asymptotic condition of $\lim_{x \to 0} C_{12}(x)/C_{23}(x) = 1$ and $\lim_{x \to L_1} C_{12}(x)/C_{23}(x) = 0$, the space-dependent coupling slits between two adjacent WGs are designed as $d_{12}(x) = d_0 e^{-(x-x_i)^2/x_c^2}$ and $d_{23}(x) = d_0 e^{-(x-x_i-\chi)^2/x_c^2}$, where $x_c = L_1/4.8$, $x_i = 2x_c$, $\chi = 0.86x_c$, and $d_0 = 343C_{\max}$. When $L_1 = 260$ mm, as illustrated in Fig. 3(e), the acoustic wave inputs from the left side of WG 1 can be transferred partially to the right side of WG 3. Following the simulated and analytical results of normalized intensity distribution shown in Fig. 3(f), the transfer efficiency in the coupler designed by AP with shortcut evolution is merely around 0.6 due to the imperfect satisfaction of adiabatic condition induced by short device length. By increasing the length of coupler to $L_1 = 360$ mm, as shown in Figs. 3(g) and 3(h), the efficiency of wave transfer is higher than that with $L_1 = 260$ mm but still lower than 0.9, indicating the drawback of the system designed by AP with shortcut evolution.

Moreover, in Fig. 4(a) we show the analytic relation between the value of β_m and the intensity of output wave from acoustic coupler designed by STAP, where the impact of discrete precision is not taken into account. It can be observed that the normalized intensity of the output wave is independent of the parameter β_m, and thus the high efficiency wave transfer from WG 1 to WG 3 can be obtained with arbitrary device length so long as the time-dependent driving pulse can be fitted well in the spatial dimension. For the acoustic coupler designed by AP with shortcut evolution, however, the device length-dependent intensity of the output wave shown in Fig. 4(b) indicates that the transfer efficiency is closely related to the coupler length. Near-perfect energy transfer from WG 1 to WG 2 can be realized only when $L_1 > 400$ mm, which is much longer than that by STAP. Therefore, compared with a traditional AP system with shortcut evolution [72], the STAP approach provides an effective way to design compact acoustic device.
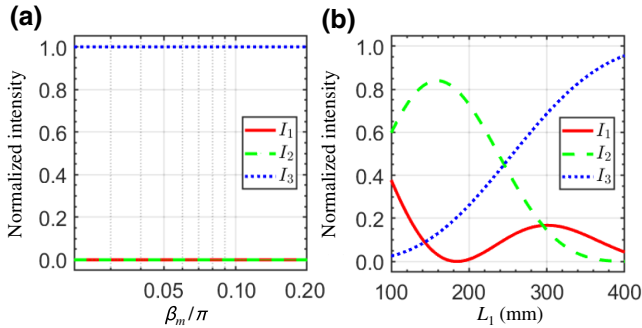
C. One-way acoustic energy transfer

As another interesting feature, the acoustic coupler designed by STAP can exhibit a one-way energy transfer. If acoustic wave is incident from the left side of WG 3, the corresponding initial condition in STAP system is $|\Psi(t_i)\rangle = |3\rangle$, and the state function follows the evolution of superposition states of $|\Psi_{\pm}(t)\rangle$ with $a_+(t_i) = a_-(t_i) = 1/\sqrt{2}$. Given by Eq. (A7), the state transfer from $|3\rangle$ to $|2\rangle$ is realized when meeting the same conditions adopted in the state transfer from $|1\rangle$ to $|3\rangle$:

$$\mu(t_i) = \mu(t_f) = 0, \quad \theta(t_i) = 0, \quad \theta(t_f) = \pi/2,$$
$$\beta_m = 0.144\pi. \tag{12}$$

By mapping the results into spatial dimension, the acoustic wave input from the left side of WG 3 can be transferred to the right side of WG 2.

Indeed, the output port for incidence from WG 3 is closely related to β_m. As numerical results show in
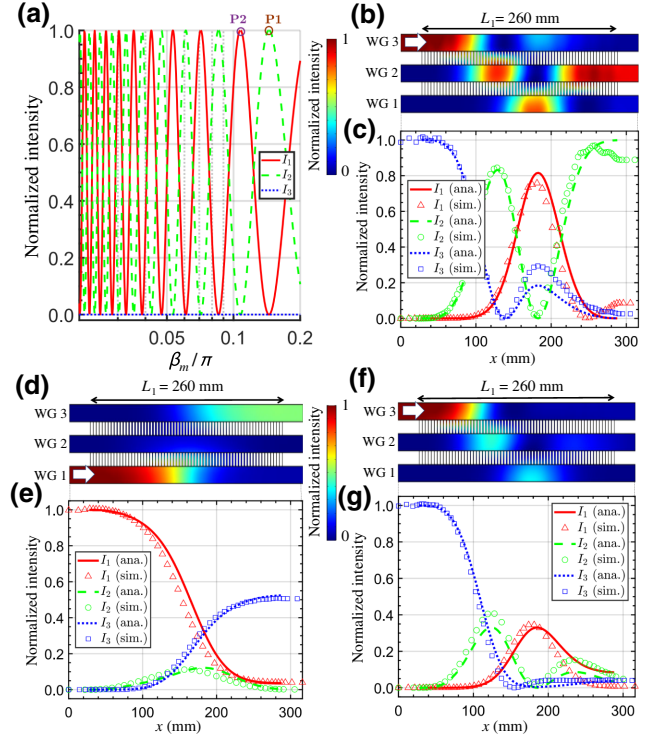
FIG. 5. (a) The relation between the intensity distributions at the output ports of three WGs and the value of β_m. The acoustic wave is incident from the left side of WG 3 at 8800 Hz. (b) The acoustic intensity field of the lossless coupler with $L_1 = 260$ mm. (c) The normalized intensity distributions along three WGs for incidence from WG 3. Acoustic intensity field of the lossy coupler with $L_1 = 260$ mm for incidences from (d) WG 1 and (f) WG 3. White arrows represent the input direction and location. The dissipation factor is $\gamma = 0.7\max[C_{12}(x)]$ in WG 2. The normalized intensity distributions along three WGs in a lossy coupler for incidence from (e) WG 1 and (g) WG 3.

FIG. 4. (a) The relation between the value of β_m and the intensity of output wave in acoustic coupler designed by STAP. (b) Device length-dependent intensity of the output wave in acoustic coupler designed by AP with shortcut evolution.

Fig. 5(a), the acoustic output intensity of the propagation wave along WG 3 can be ignored while that along the other two WGs will funnel back and forth with the increase of β_m. Therefore, either WG 1 or WG 2 can play the role of output port by selecting an appropriate value of β_m. The point marked by P2 on the red solid line corresponds to $\beta_m = 0.107\pi$ [the device shown in Fig. 3(c)]. The exchange of acoustic energy can be realized in this case because the high-intensity acoustic wave will output on WG 1 (WG 3) with incidence from WG 3 (WG 1). Meanwhile, the point marked by P1 on the green dashed line corresponds to $\beta_m = 0.144\pi$ [the device shown in Figs. 3(a) and 5(b)], which illustrates that a high-intensity acoustic wave will output on WG 2 (WG 3) with incidence from WG 3 (WG 1), providing an inspiration for a one-way acoustic energy transfer. The simulated and analytical results of acoustic intensity distribution along three WGs agree well with each other, verifying a port-selective feature of the coupler, i.e., $|1\rangle \rightarrow |3\rangle$ [Fig. 3(a)] and $|3\rangle \rightarrow |2\rangle$ [Fig. 5(b)].

Taking the acoustic coupler with $L_1 = 260$ mm as an example, the acoustic intensity distribution along WG 2 with incidence from WG 1 [Fig. 3(b)] is quite lower than that from WG 3 [Fig. 5(c)]. Hence, when we introduce a strong wave dissipation in WG 2 with a constant damping rate γ, the acoustic energy attenuation for incidence from WG 3 will be faster than that from WG 1. In this case, the coupling operator $\hat{M}(x)$ in Eq. (7) can be changed into a non-Hermitian form

$$\hat{M}_\gamma(x) = \begin{pmatrix} 0 & C_{12}(x) & 0 \\ C_{12}(x) & -i\gamma & C_{23}(x) \\ 0 & C_{23}(x) & 0 \end{pmatrix}. \quad (13)$$

The performance of lossy coupler with $L_1 = 260$ mm is illustrated in Figs. 5(d) and 5(f), from which we can observe that the normalized intensity of output wave for incidence from WG 3 (lower than 0.1) is weaker than that from WG 1 (higher than 0.5). The excellent agreement between simulated and analytical results of the intensity field shown in Figs. 5(e) and 5(g) further confirms that the output wave for incidence from WG 3 is more sensitive to lossy WG 2 than that from WG 1, and thus the acoustic coupler designed in this case has a one-way wave propagation feature. Note that the value of β_m should be as low as possible to reduce the intensity distribution along WG 2 for incidence from WG 1 so as to guarantee a high contrast ratio between WG 1 and WG 3 incidences, which is opposite to the condition for shortening the device length mentioned before. Therefore, the acoustic coupler designed in our work is a compromise, i.e., the discrete precision, device length, and one-way feature need to be taken into account simultaneously.

IV. UNIDIRECTIONAL ACOUSTIC METAMATERIAL

In this section, we intend to construct a unidirectional acoustic metamaterial based on the coupler designed by STAP, through which the incident plane acoustic wave can be split in a relatively wide space for one side incidence
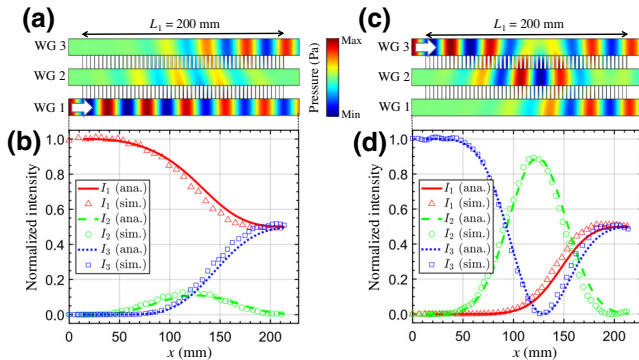

FIG. 6. Acoustic pressure field of the coupler with $L_1 = 200$ mm for incidence from (a) WG 1 and (c) WG 3. White arrows represent the input direction and location. The normalized intensity distributions along three WGs for incidence from (c) WG 1 and (d) WG 3.
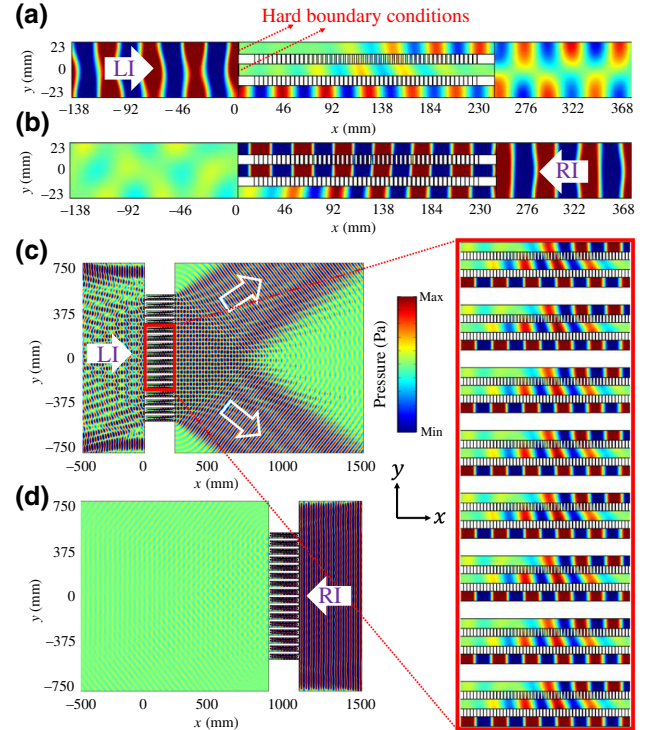

FIG. 7. Acoustic pressure fields of the unidirectional mode converter for (a) left-side incidence and (b) right-side incidence at 8800 Hz. Acoustic pressure fields of the unidirectional metamaterial composed of mode converter array for (c) left-side incidence and (d) right-side incidence at 8800 Hz.

but hardly transmitted for the other side incidence. A three-WG acoustic coupler that renders a Hadamard-like transformation, $|1\rangle \rightarrow 1/\sqrt{2}(|1\rangle - |3\rangle)$ and $|3\rangle \rightarrow 1/\sqrt{2}(|1\rangle + |3\rangle)$), is adopted to serve as a basic unit cell to generate desirable output phases for the design of metamaterial. Here, we utilize the conditions

$$\mu(x_i) = \mu(x_f) = 0, \quad \theta(x_i) = 0, \quad \theta(x_f) = \pi/4,$$
$$\beta_m = 0.107\pi \tag{14}$$

to realize the Hadamard-like wave transformation in acoustic coupler, and set $\theta_s(x) = \pi x/4x_f - 1/3 \sin(\pi x/x_f) + 1/24 \sin(2\pi x/x_f)$ and $\mu_s(x) = \beta_m/2 [1 - \cos(2\pi x/x_f)]$ for the coupling strengths in Eq. (9). The performance of acoustic coupler is shown in Figs. 6(a) and 6(c), where acoustic waves are output from WG 1 and WG 3 simultaneously with identical intensity for a single-port incidence from WG 1 or WG 3. The simulated and analytical results of intensity distribution along three WGs shown in Figs. 6(b) and 6(d) confirm the beam-splitting feature of the coupler induced by Hadamard-like wave transformation. Moreover, the phase responses of the output wave from WG 1 and WG 3 are opposite for incidence from WG 1, while those for incidence from WG 3 are the same, providing a fascinating ability to construct unidirectional acoustic device.

Before designing the acoustic metamaterial with beam-splitting feature, as shown in Figs. 7(a) and 7(b), we propose a unidirectional acoustic mode converter constructed by three coupled WGs with the left sides of WG 2 and WG 3 being sealed. For left-side incidence (LI), the 0-order plane acoustic wave can only input from the left port of WG 1, and the 1-order wave is able to be generated owing to the opposite phase responses of the output wave from WG 1 and WG 3 [34,36]. For right-side incidence (RI), however, the reflection field is strong and the transmission field is relatively weak compared with that for LI, which is attributed to the fact that most of the propagation waves along WG 1 are coupled into WG 3 and reflected by the hard boundary conditions, showing an excellent performance of unidirectional transmission feature.

Next, we adopt a coding method [90] to construct the unidirectional acoustic metamaterial with beam-splitting property, where two phase responses, 0 and π, are needed for structural design, which can be satisfied by output waves from WGs 1 and 3 due to their phase difference of π. By arraying the mode converter periodically along y direction, as shown in Fig. 7(c), a beam-splitting metamaterial is obtained, and the pattern of transmission field is determined by the period length (L_p) and the incident wavelength (λ). For LI, the diffraction of ±1-order wave are able to directly take one-pass propagation following the round-trip process demonstrated in the work [91], which is preferential to the 0-order wave, thus resulting in a splitting beam. Given the generalized Snell's law [92], the refraction angle can be calculated by $\theta_r = \arcsin(\lambda/L_p)$, which makes it necessary to guarantee the relation of $L_p > \lambda$. Otherwise, surface acoustic wave will be produced along y direction [93] and the desirable high-intensity splitting beam is not able to be obtained in this case. To avoid the generation of evanescent wave, we set $L_p = 0.064$ m, which is longer than wavelength $\lambda = (343 \text{ m/s})/(8800 \text{ Hz}) = 0.039$ m. As illustrated in Fig. 7(c), the normally incident plane wave can radiate into two directions with $\theta_r = \pm37.5°$, showing an excellent
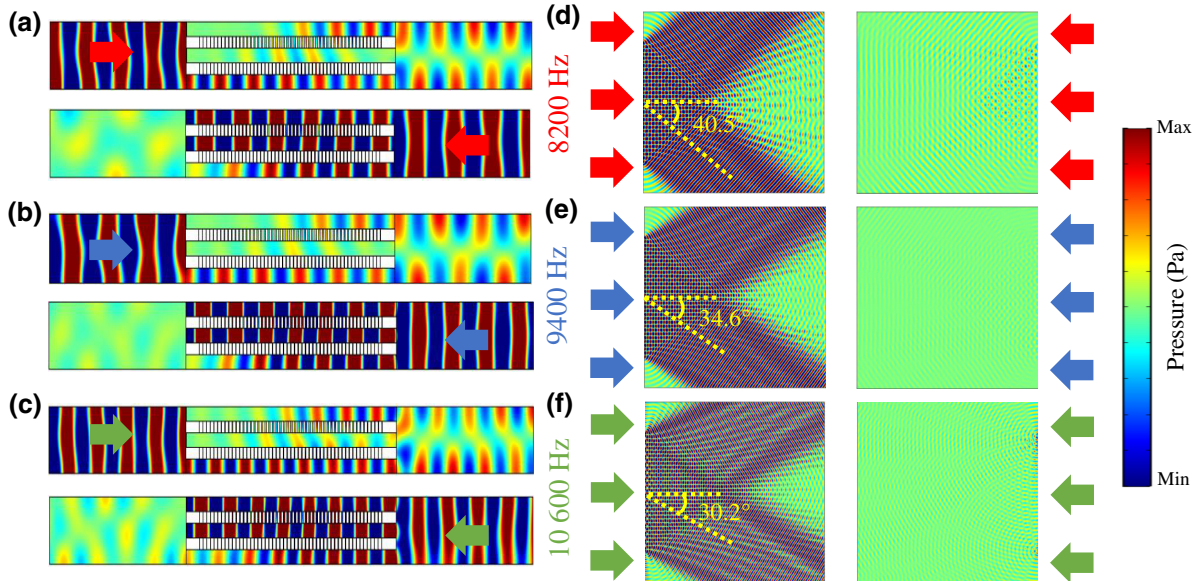

FIG. 8. Acoustic pressure fields of the mode converter and metamaterial at (a),(d) 8200 Hz, (b),(e) 9400 Hz, (c),(f) 10 600 Hz. The colored arrows represent the incident directions.

performance of beam splitting. For RI, however, the intensity of transmission field is weak owing to the strong reflection induced by mode converter array. As illustrated in Fig. 7(d), no apparent beam splitting can be observed, which confirms the unidirectional feature of the acoustic metamaterial proposed in our work.

Note that there are numerous achievements in the field of acoustic metamaterial so far. From the perspective of structural design, however, traditional approaches mainly utilize complicated unit design with resonance feature to achieve desirable phase responses, which result in unavoidable complexity of modeling and analysis. By taking advantage of the Hadamard-like acoustic transformation, our work provides a solution to construct acoustic metamaterial with a simple means (slotting the rigid material periodically). Furthermore, the dependence on resonance response makes the bandwidth being a limitation for application of the traditional device, while the acoustic device designed by STAP relies on the coupling effect rather than resonance effect. Consequently, an excellent robustness to the incident wavelength can be realized here. The broadband feature of the three-WG coupler has been illustrated in Appendix B. Therefore, as shown in Figs. 8(a)–8(f), the unidirectional acoustic mode converter and metamaterial can work well at 8200, 9400, and 10 600 Hz, verifying the broadband feature of our design. Meanwhile, the refraction angle marked in Figs. 8(d)–8(f) for LI reduces with the increase of working frequency following the relation of $\theta_r = \arcsin(\lambda/L_p)$, which indicates that the incident wavelength can be regarded as a degree of freedom to modulate the angle of splitting beam dynamically.

V. CONCLUSION

An approach is exhibited in this work for efficient transfer of acoustic wave energy by connecting shortcut to adiabatic passage with the construction of a compact acoustic coupler, expanding applications of STAP into the field of acoustics. The acoustic wave propagating along the coupler mimics the evolution of STAP for a quantum three-level system by modulating the coupling strength between two adjacent waveguides, thus resulting in a desirable behavior of energy exchange with one-way feature. Meanwhile, we further illustrate that a unidirectional acoustic mode converter is able to be designed via a three-WG coupler rendering a Hadamard-like wave transformation. Thereafter, a broadband acoustic metamaterial with simultaneous unidirectional transmission feature and the beam-splitting property can be designed by following the generalized Snell's law through periodically arraying the acoustic mode converter, which improves the practicability of the device in engineering applications including sound isolation, communication, and stealth. Our work, by introducing STAP into constructing acoustic coupler as well as acoustic metamaterial, paves a way to guide the design of advanced acoustic functional device from the behind physical laws.

APPENDIX A: TIME-DEPENDENT STAP METHOD OF DRESSED STATES IN A QUANTUM THREE-LEVEL SYSTEM

To offset nonadiabatic errors when the adiabatic criterion is not satisfied well, a correction Hamiltonian $\hat{H}_c(t)$ is needed to modify Hamiltonian (1) as $\hat{H}_{\mathrm{mod}}(t) = \hat{H}(t) + \hat{H}_c(t)$, and a unitary $\hat{V}(t)$ selecting a basis of dressed states is required to guarantee the agreement between dressed medium states and original medium states [i.e., eigenstates of Hamiltonian (1)] at instants t_i and t_f. Here, the construction of dressed states is parametrized as a rotation of the spin with Euler angles $\xi(t)$, $\mu(t)$, and $\eta(t)$ [87]

$$\hat{V}_g = \exp\left[i\eta(t)\hat{M}_z\right] \exp\left[i\mu(t)\hat{M}_x\right] \exp\left[i\xi(t)\hat{M}_z\right]. \quad \text{(A1)}$$

The correction Hamiltonian $\hat{H}_c(t)$ is given by a general form as

$$\hat{H}_c(t) = \hat{U}_{\mathrm{ad}}^{\dagger}(t)\left[g_x(t)\hat{M}_x + g_z(t)\hat{M}_z\right]\hat{U}_{\mathrm{ad}}(t), \quad \text{(A2)}$$

which leads to a modified Hamiltonian with the same form as Hamiltonian (1)

$$\hat{H}_{\mathrm{mod}} = \begin{pmatrix} 0 & \Omega_{12}^m(t) & 0 \\ \Omega_{12}^m(t) & 0 & \Omega_{23}^m(t) \\ 0 & \Omega_{23}^m(t) & 0 \end{pmatrix}, \quad \text{(A3)}$$

with $\Omega_{12}^m(t) = \Omega(t)\sin\theta(t) - g_x(t)\cos\theta(t) + g_z(t)\sin\theta(t)$, and $\Omega_{23}^m(t) = -\Omega(t)\cos\theta(t) - g_z(t)\cos\theta(t) - g_x(t)\sin\theta(t)$. Meanwhile, the Hamiltonian in the frame defined by $\hat{V}(t)$ takes the form of Patrice

$$\hat{H}_v(t) = \hat{V}(t)\hat{H}_{\mathrm{ad}}(t)\hat{V}(t)^{\dagger} + \hat{V}(t)\hat{U}(t)\hat{H}_c(t)\hat{U}(t)^{\dagger}\hat{V}(t)^{\dagger}$$
$$+ i\frac{d\hat{V}(t)}{dt}\hat{V}(t)^{\dagger}, \quad \text{(A4)}$$

in which the unwanted off-diagonal elements should be canceled to offset nonadiabatic errors. Thus the parameters

of $g_x(t)$ and $g_z(t)$ can be determined by

$$g_x(t) = \frac{\dot{\mu}(t)}{\cos \xi(t)} - \dot{\theta}(t) \tan \xi(t), \qquad \text{(A5a)}$$

$$g_z(t) = -\Omega(t) + \dot{\xi}(t) + \frac{\dot{\mu}(t) \sin \xi(t) - \dot{\theta}(t)}{\tan \mu(t) \cos \xi(t)}. \qquad \text{(A5b)}$$

For simplicity, $\xi(t) = 0$ is adopted in this work. In this situation, Hamiltonian (A4) is diagonal in the representation of the following three dressed states:

$$
\begin{aligned}
|\Psi_0(t)\rangle &= \cos \mu(t)[\cos \theta(t)|1\rangle + \sin \theta(t)|3\rangle] \\
&\quad + i \sin \mu(t)|2\rangle, \\
|\Psi_\pm(t)\rangle &= \{[\sin \theta(t) \mp i \sin \mu(t) \cos \theta(t)]|1\rangle \mp \cos \mu(t)|2\rangle \\
&\quad - [\cos \theta(t) \pm i \sin \mu(t) \sin \theta(t)]|3\rangle\} / \sqrt{2}. \quad \text{(A6)}
\end{aligned}
$$

The state function of the system can be mapped into the dressed-state space by

$$|\Psi(t)\rangle = \sum_{n=\pm,0} \tilde{a}_n(t)|\Psi_n(t)\rangle, \qquad \text{(A7)}$$

where $\tilde{a}_n(t) = a_n(t_i) \exp\left[-i \int_{t_i}^{t} \varepsilon_n(t')\, dt'\right]$ with $a_n(t_i) = \langle \Psi_n(t_i)|\Psi(t_i)\rangle$ and $\varepsilon_n(t) = \langle \Psi_n(t)|\hat{H}_{\text{mod}}(t)|\Psi_n(t)\rangle$. For a given condition of $|a_0(t_i)| = 1$ and $a_+(t_i) = a_-(t_i) = 0$, the state function follows the evolution of $|\Psi_0(t)\rangle$. Perfect state transfer from $|1\rangle$ to $|3\rangle$ can be achieved when $\mu(t)$ and $\theta(t)$ meet the condition of

$$\mu(t_i) = \mu(t_f) = 0, \quad \theta(t_i) = 0, \quad \theta(t_f) = \pi/2. \quad \text{(A8)}$$

In this case, the adiabatic criterion can be avoided and the same result of the final state as $|\psi_0(t_f)\rangle$ can be achieved by designing $\mu(t)$ and $\theta(t)$ meticulously, resulting in a shorter time of perfect evolution.

According to the analogy between two Hamiltonians (1) and (A3), it can be seen that the driving pulses in three-level system for STAP are changed to

$$
\begin{aligned}
\Omega'_{12}(t) &= -\dot{\theta}(t) \sin \theta(t) \cot \mu(t) - \dot{\mu}(t) \cos \theta(t), \\
\Omega'_{23}(t) &= \dot{\theta}(t) \cos \theta(t) \cot \mu(t) - \dot{\mu}(t) \sin \theta(t).
\end{aligned}
\quad \text{(A9)}
$$

To meet the conditions in Eq. (A8), we set the start and end instants $t_i = 0$, $t_f = T$ and pulse parameters [86,94]:

$$
\begin{aligned}
\theta(t) &= \frac{\pi t}{2T} - \frac{1}{3} \sin\left(\frac{2\pi t}{T}\right) + \frac{1}{24} \sin\left(\frac{4\pi t}{T}\right), \\
\mu(t) &= \frac{\beta_m}{2}\left[1 - \cos\left(\frac{2\pi t}{T}\right)\right],
\end{aligned}
\quad \text{(A10)}
$$

where β_m is a parameter related to evolutive populations of $|2\rangle$. Two driving pulses $\Omega'_{12}(t)$ and $\Omega'_{23}(t)$ for STAP are related to the value of β_m. Figure 9(a) shows the time-dependent coupling strength with different values of β_m, from which we can observe that the demand for maximum coupling strength decreases when the value of β_m increases, offering a variety of options for the design of driving pulses. Meanwhile, from Fig. 9(b) we learn that a higher value of β_m results in a shorter evolution time with a fixed maximum coupling strength, making it necessary to control the value of β_m as high as possible for designing compact acoustic device. Nevertheless, as another constraint to determine the value of β_m, as described in $|\Psi_0(0)\rangle$, a high value of β_m inevitably leads to a large population along mediate state $|2\rangle$. Although the loss caused by population along intermediate state can be neglected in the WG system compared with that in the system designed by quantum adiabatic technology, it would have influence on the one-way feature of the acoustic WG system (see Sec. III C). Therefore, a compromise consideration is needed to determine the value of β_m. For the initial time $t_i = 0$, Eq. (A10) could agree well with the condition (A8), providing a practical approach to STAP, so as to design a compact acoustic device.
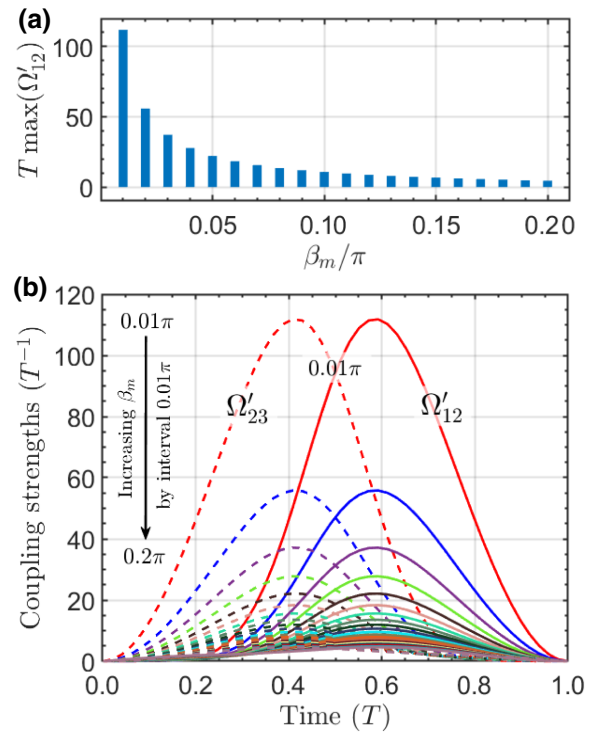

FIG. 9. (a) Time-dependent coupling strength with different values of β_m. The solid lines and dotted lines represent the driving pulses $\Omega'_{12}(t)$ and $\Omega'_{23}(t)$, respectively. (b) The relation between the values of β_m and $T\max[\Omega'_{12}(t)]$.
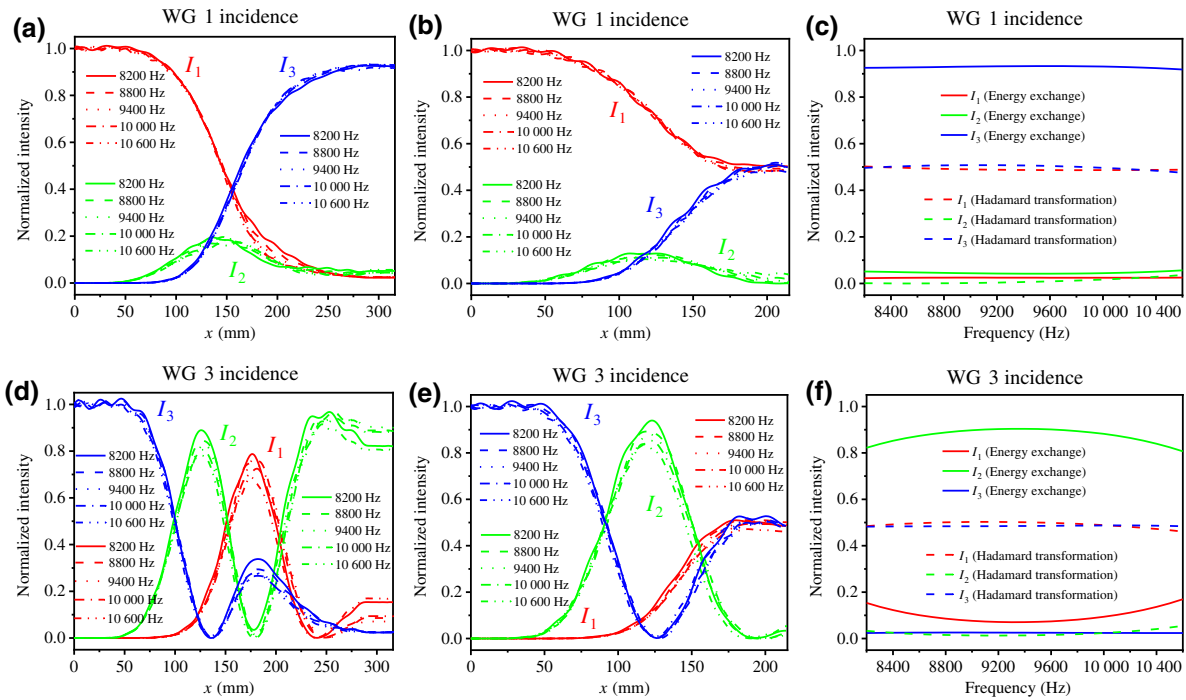
FIG. 10.   Acoustic intensity distributions along three WGs at 8200–10 600 Hz for (a),(b) WG-1 incidence and (d),(e) WG-3 incidence. Energy exchange is realized in (a),(d), and Hadamard transformation is realized in (b),(e). The transmission spectra of three WGs within 8200–10 600 Hz for (c) WG-1 incidence and (f) WG-3 incidence.

APPENDIX B: BROADBAND PERFORMANCE OF ACOUSTIC THREE-WG COUPLERS

In our work, we construct two types of three-WG coupler based on STAP, through which energy exchange and Hadamard transformation can be realized, respectively. For energy exchange and Hadamard transformation, the acoustic intensity distributions along three WGs at 8200–10 600 Hz with WG-1 incidence are shown in Figs. 10(a) and 10(b), respectively, while those with WG-3 incidence are shown in Figs. 10(d) and 10(e), respectively. The propagation process within the operating band from 8200 to 10 600 Hz can almost remain unchanged, verifying that the proposed couplers are robust to the incident frequency. Meanwhile, the transmission spectra of three WGs within 8200–106 00 Hz for WG-1 incidence and WG-3 incidence are shown in Figs. 10(c) and 10(f), respectively. The normalized output intensities for three WGs (1, 2, 3) in the cases of energy exchange and Hadamard transformation are about (0.03, 0.05, 0.92) and (0.49, 0.01, 0.50) on average for WG-1 incidence [Fig. 10(c)], while those are about (0.11, 0.86, 0.03) and (0.49, 0.02, 0.49) on average for WG-3 incidence [Fig. 10(f)]. The output intensities of three WGs meet the results of energy exchange and Hadamard transformation within 8200–10 600 Hz, which further confirms the broadband feature of the coupler. Therefore, as illustrated in Figs. 8(d)–8(f), the

unidirectional acoustic beam splitter composed of several couplers can work well in a continuous band within 8200–10 600 Hz.

[1] Michael A. Nielsen and Isaac L. Chuang, *Quantum Computation and Quantum Information: 10th Anniversary Edition* (Cambridge University Press, The Edinburgh Building, Cambridge CB2 8RU, UK, 2010).

[2] Theodor W. Hänsch, Nobel lecture: Passion for precision, Rev. Mod. Phys. **78**, 1297 (2006).

[3] Petr Král, Ioannis Thanopulos, and Moshe Shapiro, Colloquium: Coherently controlled adiabatic passage, Rev. Mod. Phys. **79**, 53 (2007).

[4] Nikolay V. Vitanov, Andon A. Rangelov, Bruce W. Shore, and Klaas Bergmann, Stimulated Raman adiabatic passage in physics, chemistry, and beyond, Rev. Mod. Phys. **89**, 015006 (2017).

[5] N. V. Vitanov, K-A Suominen, and B. W. Shore, Creation of coherent atomic superpositions by fractional stimulated Raman adiabatic passage, J. Phys. B-At. Mol. Opt. Phys. **32**, 4535 (1999).

[6] A. D. Boozer, Stimulated Raman adiabatic passage in a multilevel atom, Phys. Rev. A **77**, 023411 (2008).

[7] R. G. Unanyan, B. W. Shore, and K. Bergmann, Preparation of an n-component maximal coherent superposition state using the stimulated Raman adiabatic passage method, Phys. Rev. A **63**, 043401 (2001).

[8] G. Dridi, S. Guérin, V. Hakobyan, H. R. Jauslin, and H. Eleuch, Ultrafast stimulated Raman parallel adiabatic passage by shaped pulses, Phys. Rev. A **80,** 043408 (2009).

[9] Mustafa Demirplak and Stuart A. Rice, On the consistency, extremal, and global properties of counterdiabatic fields, J. Chem. Phys. **129,** 154111 (2008).

[10] M. V. Berry, Transitionless quantum driving, J. Phys. A-Math. Theor. **42,** 365303 (2009).

[11] Xi Chen, I. Lizuain, A. Ruschhaupt, D. Guéry-Odelin, and J. G. Muga, Shortcut to Adiabatic Passage in Two- and Three-Level Atoms, Phys. Rev. Lett. **105,** 123003 (2010).

[12] D. Guéry-Odelin, A. Ruschhaupt, A. Kiely, E. Torrontegui, S. Martínez-Garaot, and J. G. Muga, Shortcuts to adiabaticity: Concepts, methods, and applications, Rev. Mod. Phys. **91,** 045001 (2019).

[13] Brian B. Zhou, Alexandre Baksic, Hugo Ribeiro, Christopher G. Yale, F. Joseph Heremans, Paul C. Jerger, Adrian Auer, Guido Burkard, Aashish A. Clerk, and David D. Awschalom, Accelerated quantum control using superadiabatic dynamics in a solid-state lambda system, Nat. Phys. **13,** 330 (2017).

[14] Antti Vepsäläinen, Sergey Danilin, and Gheorghe Sorin Paraoanu, Superadiabatic population transfer in a three-level superconducting circuit, Sci. Adv. **5,** eaau5999 (2019).

[15] Tongxing Yan, Bao-Jie Liu, Kai Xu, Chao Song, Song Liu, Zhensheng Zhang, Hui Deng, Zhiguang Yan, Hao Rong, Keqiang Huang, Man-Hong Yung, Yuanzhen Chen, and Dapeng Yu, Experimental Realization of Nonadiabatic Shortcut to Non-Abelian Geometric Gates, Phys. Rev. Lett. **122,** 080501 (2019).

[16] Ji Chu, Danyu Li, Xiaopei Yang, Shuqing Song, Zhikun Han, Zhen Yang, Yuqian Dong, Wen Zheng, Zhimin Wang, Xiangmin Yu, Dong Lan, Xinsheng Tan, and Yang Yu, Realization of Superadiabatic Two-Qubit Gates using Parametric Modulation in Superconducting Circuits, Phys. Rev. Appl. **13,** 064012 (2020).

[17] Ye-Hong Chen, Wei Qin, Xin Wang, Adam Miranowicz, and Franco Nori, Shortcuts to Adiabaticity for the Quantum Rabi Model: Efficient Generation of Giant Entangled Cat States via Parametric Amplification, Phys. Rev. Lett. **126,** 023602 (2021).

[18] Tzung-Yi Lin, Fu-Chen Hsiao, Yao-Wun Jhang, Chieh Hu, and Shuo-Yen Tseng, Mode conversion using optical analogy of shortcut to adiabatic passage in engineered multimode waveguides, Opt. Express **20,** 24085 (2012).

[19] S. Martínez-Garaot, Shuo-Yen Tseng, and J. G. Muga, Compact and high conversion efficiency mode-sorting asymmetric Y junction using shortcuts to adiabaticity, Opt. Lett. **39,** 2306 (2014).

[20] Wei Huang, Shi-Jun Liang, Elica Kyoseva, and Lay Kee Ang, Adiabatic control of surface plasmon-polaritons in a 3-layers graphene curved configuration, Carbon **127,** 187 (2018).

[21] H.-C. Chung, S. Martínez-Garaot, X. Chen, J. G. Muga, and S.-Y. Tseng, Shortcuts to adiabaticity in optical waveguides, EPL (Europhysics Letters) **127,** 34001 (2019).

[22] Adam K. Taras, Alessandro Tuniz, Musawer A. Bajwa, Vincent Ng, Judith M. Dawes, Christopher G. Poulton, and C. Martijn De Sterke, Shortcuts to adiabaticity in waveguide couplers–theory and implementation, Adv. Phys. X **6,** 1894978 (2021).

[23] S. González-Resines, D. Guéry-Odelin, A. Tobalina, I. Lizuain, E. Torrontegui, and J. G. Muga, Invariant-Based Inverse Engineering of Crane Control Parameters, Phys. Rev. Appl. **8,** 054008 (2017).

[24] Daniel Martínez-Cercós, David Guéry-Odelin, and Juan Gonzalo Muga, Robust load transport by an overhead crane with respect to cable length uncertainties, J. Vib. Control **26,** 1514 (2020).

[25] Nikolay V. Vitanov and Michael Drewsen, Highly Efficient Detection and Separation of Chiral Molecules through Shortcuts to Adiabaticity, Phys. Rev. Lett. **122,** 173202 (2019).

[26] Jin-Lei Wu, Yan Wang, Jie Song, Yan Xia, Shi-Lei Su, and Yong-Yuan Jiang, Robust and highly efficient discrimination of chiral molecules through three-mode parallel paths, Phys. Rev. A **100,** 043413 (2019).

[27] Daniel M. Weinreich, Herding an evolving biological population with quantum control tools, Nat. Phys. **17,** 17 (2021).

[28] S. Iram, E. Dolson, J. Chiel, J. Pelesko, N. Krishnan, Ö. Güngör, B. Kuznets-Speck, S. Deffner, E. Ilker, J. G. Scott, and M. Hinczewski, Controlling the speed and trajectory of evolution with counterdiabatic driving, Nat. Phys. **17,** 135 (2021).

[29] Wen Kang Cao, Cheng Zhang, Li Ting Wu, Kai Qi Guo, Jun Chen Ke, Tie Jun Cui, and Qiang Cheng, Tunable Acoustic Metasurface for Three-Dimensional Wave Manipulations, Phys. Rev. Appl. **15,** 024026 (2021).

[30] Sheng-Dong Zhao, A-Li Chen, Yue-Sheng Wang, and Chuanzeng Zhang, Continuously Tunable Acoustic Metasurface for Transmitted Wavefront Modulation, Phys. Rev. Appl. **10,** 054066 (2018).

[31] Shuai Tang, Rui Wang, Jianning Han, and Yongyuan Jiang, Acoustic energy transport characteristics based on amplitude and phase modulation using waveguide array, J. Appl. Phys. **128,** 165103 (2020).

[32] Jin-Lei Wu, Shuai Tang, Yan Wang, XiaoSai Wang, Jin-Xuan Han, Cheng Lü, Jie Song, Shi-Lei Su, Yan Xia, and YongYuan Jiang, Unidirectional acoustic metamaterials based on nonadiabatic holonomic quantum transformations, Sci. China-Phys. Mech. Astron. **65,** 220311 (2021).

[33] Guofu Xu, A bridge between acoustic metamaterials and quantum computation, Sci. China-Phys. Mech. Astron. **65,** 240331 (2022).

[34] Shuai Tang, Bin Ren, Yuxin Feng, Jie Song, and Yongyuan Jiang, Asymmetric acoustic beam shaping based on monolayer binary metasurfaces, Appl. Phys. Express **14,** 085504 (2021).

[35] Jie Zhu, Xuefeng Zhu, Xiaobo Yin, Yuan Wang, and Xiang Zhang, Unidirectional Extraordinary Sound Transmission with Mode-Selective Resonant Materials, Phys. Rev. Appl. **13,** 041001 (2020).

[36] Jiao Qian, Yin Wang, Jian-ping Xia, Yong Ge, Shou-qi Yuan, Hong-xiang Sun, and Xiao-jun Liu, Broadband integrative acoustic asymmetric focusing lens based on mode-conversion meta-atoms, Appl. Phys. Lett. **116,** 223505 (2020).

[37] Xuefeng Zhu, Kun Li, Peng Zhang, Jie Zhu, Jintao Zhang, Chao Tian, and Shengchun Liu, Implementation of dispersion-free slow acoustic wave propagation and

phase engineering with helical-structured metamaterials, Nat. Commun. **7,** 11731 (2016).

[38] Jin Zhang, Ye Tian, Ying Cheng, and Xiaojun Liu, Acoustic holography using composite metasurfaces, Appl. Phys. Lett. **116,** 030501 (2020).

[39] Cheng Zhang, Wen Kang Cao, Li Ting Wu, Jun Chen Ke, Yun Jing, Tie Jun Cui, and Qiang Cheng, A reconfigurable active acoustic metalens, Appl. Phys. Lett. **118,** 133502 (2021).

[40] R. Menchon-Enrich, J. Mompart, and V. Ahufinger, Spatial adiabatic passage processes in sonic crystals with linear defects, Phys. Rev. B **89,** 094304 (2014).

[41] Ze-Guo Chen and Ying Wu, Tunable Topological Phononic Crystals, Phys. Rev. Appl. **5,** 054021 (2016).

[42] Xue-Feng Li, Xu Ni, Liang Feng, Ming-Hui Lu, Cheng He, and Yan-Feng Chen, Tunable Unidirectional Sound Propagation through a Sonic-Crystal-Based Acoustic Diode, Phys. Rev. Lett. **106,** 084301 (2011).

[43] Yong Li, Shuibao Qi, and M. Badreddine Assouar, Theory of metascreen-based acoustic passive phased array, New J. Phys. **18,** 043024 (2016).

[44] Guang-Sheng Liu, Yao-Yin Peng, Ming-Hao Liu, Xin-Ye Zou, and Jian-Chun Cheng, Broadband acoustic energy harvesting metasurface with coupled Helmholtz resonators, Appl. Phys. Lett. **113,** 153503 (2018).

[45] H. Ryoo and W. Jeon, Perfect sound absorption of ultra-thin metasurface based on hybrid resonance and space-coiling, Appl. Phys. Lett. **113,** 121903 (2018).

[46] Yong Li, Bin Liang, Xin-Ye Zou, and Jian-Chun Cheng, Extraordinary acoustic transmission through ultrathin acoustic metamaterials by coiling up space, Appl. Phys. Lett. **103,** 063509 (2013).

[47] Hussein Esfahlani, Herve Lissek, and Juan R. Mosig, Generation of acoustic helical wavefronts using metasurfaces, Phys. Rev. B **95,** 024312 (2017).

[48] Weibai Li, and Fei Meng, and Xiaodong Huang, Coding metalens with helical-structured units for acoustic focusing and splitting, Appl. Phys. Lett. **117,** 021901 (2020).

[49] Huifang Xie and Zhilin Hou, Nonlocal Metasurface for Acoustic Focusing, Phys. Rev. Appl. **15,** 034054 (2021).

[50] Shu Zhang, Leilei Yin, and Nicholas Fang, Focusing Ultrasound with an Acoustic Metamaterial Network, Phys. Rev. Lett. **102,** 194301 (2009).

[51] Shuai Tang, Bin Ren, Yuxin Feng, Jie Song, and Yongyuan Jiang, Broadband acoustic focusing via binary rectangular cavity/Helmholtz resonator metasurface, J. Appl. Phys. **129,** 155307 (2021).

[52] Bingyi Liu, Zhaoxian Su, Yong Zeng, Yongtian Wang, Lingling Huang, and Shuang Zhang, Acoustic geometric-phase meta-array, New J. Phys. **23,** 113026 (2021).

[53] Shuai Tang, Cheng Lü, Jin-Lei Wu, Jie Song, and Yongyuan Jiang, Wavelength-selected bifunctional beam shaping for transmitted acoustic waves via coding metasurface, Appl. Acoust. **194,** 108786 (2022).

[54] Xiao-Shuang Li, Hong-Tao Zhou, Yan-Feng Wang, and Yue-Sheng Wang, Modulation of acoustic self-accelerating beams with tunable curved metasurfaces, Appl. Phys. Lett. **118,** 023503 (2021).

[55] Shuai Tang, Bin Ren, Yuxin Feng, Jie Song, and Yongyuan Jiang, The generation of acoustic airy beam with selective band based on binary metasurfaces: Customized on demand, Appl. Phys. Lett. **119,** 071907 (2021).

[56] Xue Jiang, Yong Li, Bin Liang, Jian-chun Cheng, and Likun Zhang, Convert Acoustic Resonances to Orbital Angular Momentum, Phys. Rev. Lett. **117,** 034301 (2016).

[57] Xuemei Ren, Qinxin Zhou, Zheng Xu, and Xiaojun Liu, Particle Trapping in Arbitrary Trajectories using First-Order Bessel-like Acoustic Beams, Phys. Rev. Appl. **15,** 054041 (2021).

[58] Xu-Dong Fan and Likun Zhang, Trapping Force of Acoustical Bessel Beams on a Sphere and Stable Tractor Beams, Phys. Rev. Appl. **11,** 014055 (2019).

[59] Zhiwang Zhang, Qi Wei, Ying Cheng, Ting Zhang, Dajian Wu, and Xiaojun Liu, Topological Creation of Acoustic Pseudospin Multipoles in a Flow-Free Symmetry-Broken Metamaterial Lattice, Phys. Rev. Lett. **118,** 084303 (2017).

[60] Taehwa Lee and Hideo Iizuka, Bragg scattering based acoustic topological transition controlled by local resonance, Phys. Rev. B **99,** 064305 (2019).

[61] Haoran Xue, Yahui Yang, Guigeng Liu, Fei Gao, Yidong Chong, and Baile Zhang, Realization of an Acoustic Third-Order Topological Insulator, Phys. Rev. Lett. **122,** 244301 (2019).

[62] Cheng He, Hua-Shan Lai, Bo He, Si-Yuan Yu, Xiangyuan Xu, Ming-Hui Lu, and Yan-Feng Chen, Hybrid acoustic topological insulator in three dimensions, Nat. Commun. **11,** 2318 (2020).

[63] Jian-Ping Xia, Ding Jia, Hong-Xiang Sun, Shou-Qi Yuan, Yong Ge, and Qiao-Rui Si, and Xiao-Jun Liu, Programmable coding acoustic topological insulator, Adv. Mater. **30,** 1805002 (2018).

[64] Qiang Wang, Yong Ge, Hong-Xiang Sun, Haoran Xue, Ding Jia, Yi-Jun Guan, Shou-Qi Yuan, Baile Zhang, and Y. D. Chong, Vortex states in an acoustic Weyl crystal with a topological lattice defect, Nat. Commun. **12,** 3654 (2021).

[65] Yuzhen Yang, Han Jia, Yafeng Bi, Han Zhao, and Jun Yang, Experimental Demonstration of an Acoustic Asymmetric Diffraction Grating Based on Passive Parity-Time-Symmetric Medium, Phys. Rev. Appl. **12,** 034040 (2019).

[66] Jun Lan, Liwei Wang, Xiaowei Zhang, Minghui Lu, and Xiaozhou Liu, Acoustic Multifunctional Logic Gates and Amplifier Based on Passive Parity-Time Symmetry, Phys. Rev. Appl. **13,** 034047 (2020).

[67] Romain Fleury, Dimitrios Sounas, and Andrea Alù, An invisible acoustic sensor based on parity-time symmetry, Nat. Commun. **6,** 5905 (2015).

[68] Xuefeng Zhu, Hamidreza Ramezani, Chengzhi Shi, Jie Zhu, and Xiang Zhang, $\mathcal{PT}$-Symmetric Acoustics, Phys. Rev. X **4,** 031042 (2014).

[69] Ya-Xi Shen, Long-Sheng Zeng, Zhi-Guo Geng, De-Gang Zhao, Yu-Gui Peng, Jie Zhu, and Xue-Feng Zhu, Acoustic topological adiabatic passage via a level crossing, Sci. China-Phys. Mech. Astron. **64,** 244302 (2020).

[70] Long-Sheng Zeng, Ya-Xi Shen, Yu-Gui Peng, De-Gang Zhao, and Xue-Feng Zhu, Selective Topological Pumping for Robust, Efficient, and Asymmetric Sound Energy Transfer in a Dynamically Coupled Cavity Chain, Phys. Rev. Appl. **15,** 064018 (2021).

[71] Ya-Xi Shen, Long-Sheng Zeng, Zhi-Guo Geng, De-Gang Zhao, Yu-Gui Peng, and Xue-Feng Zhu, Acoustic Adiabatic Propagation Based on Topological Pumping in a Coupled Multicavity Chain Lattice, Phys. Rev. Appl. **14,** 014043 (2020).

[72] Ya-Xi Shen, Yu-Gui Peng, De-Gang Zhao, Xin-Cheng Chen, Jie Zhu, and Xue-Feng Zhu, One-way Localized Adiabatic Passage in an Acoustic System, Phys. Rev. Lett. **122,** 094501 (2019).

[73] Ze-Guo Chen, Weiyuan Tang, Ruo-Yang Zhang, Zhaoxian Chen, and Guancong Ma, Landau-Zener Transition in the Dynamic Transfer of Acoustic Topological States, Phys. Rev. Lett. **126,** 054301 (2021).

[74] Albert Messiah, *Quantum Mechanics* (North-Holland, Amsterdam, 1962).

[75] Y. O. Dudin and A. Kuzmich, Strongly interacting Rydberg excitations of a cold atomic gas, Science **336,** 887 (2012).

[76] K. Bergmann, H. Theuer, and B. W. Shore, Coherent population transfer among quantum states of atoms and molecules, Rev. Mod. Phys. **70,** 1003 (1998).

[77] Shuai Tang, Jin-Lei Wu, Cheng Lü, Xiaosai Wang, Jie Song, and Yongyuan Jiang, Acoustic wavelength-selected metamaterials designed by reversed fractional stimulated Raman adiabatic passage, Phys. Rev. B **105,** 104107 (2022).

[78] S. Longhi, G. Della Valle, M. Ornigotti, and P. Laporta, Coherent tunneling by adiabatic passage in an optical waveguide system, Phys. Rev. B **76,** 201101 (2007).

[79] R. Menchon-Enrich, A. Benseny, V. Ahufinger, A. D. Greentree, Th. Busch, and J. Mompart, Spatial adiabatic passage: A review of recent progress, Rep. Prog. Phys. **79,** 074401 (2016).

[80] H. R. Lewis and W. B. Riesenfeld, An exact quantum theory of the time-dependent harmonic oscillator and of a charged particle in a time-dependent electromagnetic field, J. Math. Phys. **10,** 1458 (1969).

[81] Xi Chen and J. G. Muga, Engineering of fast population transfer in three-level systems, Phys. Rev. A **86,** 033405 (2012).

[82] S. Ibáñez, Xi Chen, and J. G. Muga, Improving shortcuts to adiabaticity by iterative interaction pictures, Phys. Rev. A **87,** 043402 (2013).

[83] Xue-Ke Song, Qing Ai, Jing Qiu, and Fu-Guo Deng, Physically feasible three-level transitionless quantum driving with multiple schrödinger dynamics, Phys. Rev. A **93,** 052324 (2016).

[84] Yi-Hao Kang, Ye-Hong Chen, Qi-Cheng Wu, Bi-Hua Huang, Yan Xia, and Jie Song, Reverse engineering of a Hamiltonian by designing the evolution operators, Sci. Rep. **6,** 30151 (2016).

[85] Ye-Hong Chen, Qi-Cheng Wu, Bi-Hua Huang, Jie Song, and Yan Xia, Arbitrary quantum state engineering in three-state systems via counterdiabatic driving, Sci. Rep. **6,** 38484 (2016).

[86] Jin-Lei Wu, Xin Ji, and Shou Zhang, Shortcut to adiabatic passage in a three-level system via a chosen path and its application in a complicated system, Opt. Express **25,** 21084 (2017).

[87] Alexandre Baksic, Hugo Ribeiro, and Aashish A. Clerk, Speeding up Adiabatic Quantum State Transfer by using Dressed States, Phys. Rev. Lett. **116,** 230503 (2016).

[88] Bao-Jie Liu, Zhen-Hua Huang, Zheng-Yuan Xue, and Xin-Ding Zhang, Superadiabatic holonomic quantum computation in cavity QED, Phys. Rev. A **95,** 062308 (2017).

[89] Ya-Xi Shen, Yu-Gui Peng, Xin-Cheng Chen, De-Gang Zhao, and Xue-Feng Zhu, Observation of low-loss broadband supermode propagation in coupled acoustic waveguide complex, Sci. Rep. **7,** 45603 (2017).

[90] Boyang Xie, Kun Tang, Hua Cheng, Zhengyou Liu, Shuqi Chen, and Jianguo Tian, Coding acoustic metasurfaces, Adv. Mater. **29,** 1603507 (2017).

[91] Yangyang Fu, Chen Shen, Yanyan Cao, Lei Gao, Huanyang Chen, C. T. Chan, Steven A. Cummer, and Yadong Xu, Reversal of transmission and reflection based on acoustic metagratings with integer parity design, Nat. Commun. **10,** 2326 (2019).

[92] Nanfang Yu, Patrice Genevet, Mikhail A. Kats, Francesco Aieta, Jean-Philippe Tetienne, Federico Capasso, and Zeno Gaburro, Light propagation with phase discontinuities: Generalized laws of reflection and refraction, Science **334,** 333 (2011).

[93] Jun Mei and Ying Wu, Controllable transmission and total reflection through an impedance-matched acoustic metasurface, New J. Phys. **16,** 123007 (2014).

[94] Yi-Hao Kang, Ye-Hong Chen, Zhi-Cheng Shi, Jie Song, and Yan Xia, Fast preparation of *w* states with superconducting quantum interference devices by using dressed states, Phys. Rev. A **94,** 052311 (2016).